

Role of active stress and actin alignment in cell division:A hydrodynamic perspective

Kunhao Dong(董堃昊), Menglong Feng(冯梦龙), and Rui Ma(马锐)

Citation: Chin. Phys. B, 2025, 34 (**8**): 088705. DOI: 10.1088/1674-1056/adcd44
http://cpb.iphy.ac.cn; http://iopscience.iop.org/cpb

What follows is a list of articles you may be interested in

Depolymerization mechanism of microtubule revealed by nucleotide-dependent changes of longitudinal and lateral interactions

Bingbing Zhang(张冰冰), Ziling Huo(霍子玲), Jiaxi Li(李佳希), Jingyu Qin(覃静宇), and Yizhao Geng(耿轶钊)
Chin. Phys. B, 2025, 34 (**6**): 068702. DOI: 10.1088/1674-1056/adc369

Cholesterol-induced deformation of the gramicidin A channel inhibiting potassium ion binding and transport

Pan Xiao(肖盼), Yu Cao(曹宇), Jin Zhu(朱瑾), and Qing Liang(梁清)
Chin. Phys. B, 2024, 33 (**5**): 058701. DOI: 10.1088/1674-1056/ad334e

Molecular dynamics simulations on the interactions between nucleic acids and a phospholipid bilayer

Yao Xu(徐耀), Shu-Wei Huang(黄舒伟), Hong-Ming Ding(丁泓铭), and Yu-Qiang Ma(马余强)
Chin. Phys. B, 2024, 33 (**2**): 028701. DOI: 10.1088/1674-1056/ad1178

A primary model of decoherence in neuronal microtubules based on the interaction Hamiltonian between microtubules and plasmon in neurons

Zuoxian Xiang(向左鲜), Chuanxiang Tang(唐传祥), Lixin Yan(颜立新)
Chin. Phys. B, 2019, 28 (**4**): 048701. DOI: 10.1088/1674-1056/28/4/048701

Propagation of kink-antikink pair along microtubules as a control mechanism for polymerization and depolymerization processes

L. Kavitha, A. Muniyappan, S. Zdravković, M. V. Satarić, A. Marlewski, S. Dhamayanthi, D. Gopi
Chin. Phys. B, 2014, 23 (**9**): 098703. DOI: 10.1088/1674-1056/23/9/098703

SPECIAL TOPIC — A celebration of the 90th Anniversary of the Birth of Bolin Hao

Role of active stress and actin alignment in cell division: A hydrodynamic perspective

Kunhao Dong(董堃昊)[1,†], Menglong Feng(冯梦龙)[1,†], and Rui Ma(马锐)[2,‡]

[1] *Department of Physics, College of Physical Science and Technology, Xiamen University, Xiamen* 361005, *China*

[2] *Fujian Provincial Key Laboratory for Soft Functional Materials Research, Research Institute for Biomimetics and Soft Matter, Department of Physics, College of Physical Science and Technology, Xiamen University, Xiamen* 361005, *China*

(Received 23 February 2025; revised manuscript received 1 April 2025; accepted manuscript online 16 April 2025)

Cell division is a fundamental biological process in which a parent cell divides into two daughter cells. The cell cortex, a thin layer primarily composed of actin filaments and myosin motors beneath the plasma membrane, plays a critical role in ensuring proper cell division. In this study, we apply a hydrodynamic model to describe the actin cortex as an active nematic surface, incorporating orientational order arising from actin filament alignment and anisotropic active stress produced by myosin motors. By analyzing the linearized dynamics, we investigate how shape, flow, and stress regulators evolve over time when the surface deviates slightly from a sphere. Our findings reveal that the active alignment of actin filaments, often overlooked in previous studies, is crucial for successful division. Furthermore, we demonstrate that a cortical chiral flow naturally emerges as a consequence of this active alignment. Overall, our results provide a mechanistic explanation for key phenomena observed during cell division, offering new insights into the role of active stress and filament alignment in cortical dynamics.

Keywords: cell division, actin cortex, nematic surface, chiral flow

PACS: 87.16.D–, 87.16.Ka, 87.17.Ee, 87.17.Pq

DOI: 10.1088/1674-1056/adcd44 **CSTR:** 32038.14.CPB.adcd44

1. Introduction

Active matter encompasses a wide range of systems and has been extensively studied in both artificial and biological contexts, where self-propulsion and self-assembly play crucial roles.[1,2] On a macroscopic scale, a typical example is bird flocks, whose collective motion and long-range diffusion differ significantly from the Brownian motion observed in equilibrium systems.[3,4] On the microscale, bacterial suspensions exhibit complex behaviors and are generally classified as pushers or pullers based on their interaction with the ambient fluid.[5,6] On both scales, activity plays an essential role in shaping the movement and pattern formation.[7–10] Despite their diversity, active matter systems can roughly be categorized into polar and nematic types based on molecular symmetry. Polar active matter consists of self-propelled particles with a preferred direction of motion, while nematic active matter consists of elongated, head–tail symmetric particles that align but move in both directions. The hydrodynamic approach, based on conservation laws and irreversible thermodynamics, is a powerful tool to describe the motion of active matters, both in flat space[11] and on curved surfaces.[12,13]

As a typical example of active matter, motor proteins regulate the cellular mechanics. They represent a class of active matter that converts chemical energy into mechanical work and are crucial in the shape of the cell.[14–16]

The cellular shape depends on two main structures, the cytoskeleton and plasma membrane. As the scaffold of a cell, the cytoskeleton, constructed by three main components: the actin filaments, microtubule, and intermediate filament, supports the cell and determines the global shape. Although the plasma membrane (about 5 nm thick) is usually treated as a fluid, it also contributes to the elastic properties[17] and electrical properties.[18,19] Theoretically, it is usually described by the Helfrich model whose free energy is determined by the deviation from the preferred curvature of a membrane.[20] Beneath the plasma membrane lies the cell cortex, which is a thin fluid layer (about 100 nm thick) composed by grid-like actin filaments connected by gel-forming proteins.[21,22]

In particular, motors can generate force or torque when connected to other structures,[23,24] especially the cytoskeleton.[25] Generally, they have three main categories: myosin, kinesin, and dynein. Each of them has characteristic motor domains that are responsible for converting the chemical energy into mechanical work. Furthermore, some of them have domains that can be connected to cargoes to carry out transport.[26]

Cell division is crucial for any cellular organism. During this process, assisted by many functional proteins, motor proteins drive the deformation of cortex and plasma mem-

[†]These authors contributed equally to this work.

[‡]Corresponding author. E-mail: ruima@xmu.edu.cn

© 2025 Chinese Physical Society and IOP Publishing Ltd. All rights, including for text and data mining, AI training, and similar technologies, are reserved.

brane. A typical phenomenon during cell division is the formation of a contractile ring, which is composed of a bundle of antiparallel actin filaments and has been thoroughly investigated in yeast cells.[27–29] After receiving signals,[30] myosin motors (usually myosin II[31]), powered by ATP hydrolysis, generate sliding of actin filaments,[32] resulting in contraction of the contractile ring.[33] Further research has indicated that myosin-IIA and myosin-IIB play different roles, the former generating cortex tension while the latter stabilizing the shape.[34] Meanwhile, various proteins participate in this intricate process, such as anillin,[35] formin,[36] Mid1,[37] cofilin,[38] Paxillin,[39] Rho family proteins,[40] F-BAR,[41] and other complexes.[42] They and their associations are believed to be responsible for the assembly and positioning of the ring, as well as the generation of force.[43–46] In addition, the connectivity of the ring affects its contractility.[47–49] The ring must be properly anchored by proteins such as Cdc15p to the membrane; otherwise it will slide away from the equator on the membrane.[50] In addition to the contractile ring, septin rings triggered by constriction are observed,[51] in which the septin is believed to increase the contractility of the actomyosin ring.[52] Both the cell cortex and the plasma membrane are strongly constricted at the cleavage furrow[53] and finally the cell is divided into two daughter cells with the help of ESCRT-III family proteins.[54]

Another phenomenon observed during cell division is chiral flow, where the cortex exhibits opposite directional flows in the two hemispheres during the early stages of division.[55,56] Computer simulations have shown that chiral flow can arise from imposed chiral force.[57] However, whether the chiral flow can spontaneously emerge from an active nematic surface remains unclear.

Extensive theoretical work has been conducted on cell division. Salbreux *et al.*[58] applied the theory of active nematics to model contractile ring formation on a cylindrical surface, showing that filament alignment within the ring at the equator results from cortical flows towards the equator due to flow-alignment coupling. However, their model did not account for surface deformation. Bell *et al.*[59] extended active nematic theory to undeformed curved surfaces, although alignment was imposed rather than emerging spontaneously. More recently, a dynamic model of epithelial shells driven by active nematics was studied in Ref. [60], demonstrating that nematic alignment influences shell shape transformation. However, when computing the nematic tensor gradient on a curved surface, its coupling with the curvature tensor was not considered. A general framework based on irreversible thermodynamics has been systematically constructed for isotropic[13] and polar/nematic[12] active surfaces. Using a minimal example from the general framework, Mietke *et al.* explored conditions for the formation of contractile rings and the polarization phenomena for isotropic active surfaces.[61,62] However, a more realistic model must incorporate the anisotropic nature of active forces, which has been demonstrated in experiments.[63]

In this work, we describe the actin cortex as an active nematic fluid surface based on the framework developed in Ref. [12]. Assuming axisymmetry of the surface shape, we study the linearized dynamics of the hydrodynamic equations. Compared with studies discussed above, the novelty of our model is summarized as follows. (1) We describe the cortex as a curved, flexible surface with active nematics, allowing for cellular deformation. (2) We employ a fully self-organized approach based on the Landau–de Gennes model of liquid crystals to reveal contractile ring formation without imposing the nematic order. (3) Our model incorporates the curvature and nematic tensor coupling when calculating the nematic tensor gradient. (4) Unlike most previous studies that typically neglect active alignment,[59,60] we find that active alignment is vital to promote cell division. (5) Instead of imposing a chiral force, chiral flows spontaneously emerge in our model as a result of active extensile (not contractile) stress.

This paper is organized as follows. In Section 2, we introduce the hydrodynamic model of the actin cortex. We study the linearized dynamics of the system around a steady state in Section 3, discuss its relevance to cell division in Section 4, and conclude the paper in Section 5.

2. Model of actin cortex

2.1. Geometry of the surface

We describe the shape of the cellular cortex as a surface that is parameterized as $\boldsymbol{X}(s^1, s^2, t)$, with the surface coordinates s^1, s^2 and the time coordinate t. The covariant tangential basis vectors are given by $\boldsymbol{g}_i = \partial_i \boldsymbol{X}$, where $\partial_i = \partial/\partial s^i$ denotes the partial derivatives with respect to the surface coordinates. The metric tensor is defined by $g_{ij} = \boldsymbol{g}_i \cdot \boldsymbol{g}_j$ and $g^{ij} g_{jk} = \delta^i_k$. Hereafter we use the Einstein summation convention for repeated upper and lower indices. The unit normal vector of the surface reads $\boldsymbol{n} = \boldsymbol{g}_1 \times \boldsymbol{g}_2 / |\boldsymbol{g}_1 \times \boldsymbol{g}_2|$. The Levi–Civita tensor ϵ_{ij} is defined by the equation $\boldsymbol{g}_i \times \boldsymbol{g}_j = \epsilon_{ij} \boldsymbol{n}$. The curvature tensor $\boldsymbol{C} = C_{ij} \boldsymbol{g}^i \otimes \boldsymbol{g}^j$, defined as the gradient of the normal vector $\boldsymbol{n}$, is given by $C_{ij} = -\boldsymbol{n} \cdot (\partial_i \boldsymbol{g}_j)$. The mean curvature of the surface is defined as the trace of the curvature tensor C^k_k.

2.2. Surface vectors and tensors

For a general vector field $\boldsymbol{a} = a^i \boldsymbol{g}_j + a_n \boldsymbol{n}$, we use the notation $\boldsymbol{a}_\parallel = a^i \boldsymbol{g}_j$ to denote its tangential components and $\boldsymbol{a}_\perp = a_n \boldsymbol{n}$ to denote its normal components. For a second-rank tensor field $\boldsymbol{B} = B^{ij} \boldsymbol{g}_i \otimes \boldsymbol{g}_j + B^i_n \boldsymbol{g}_i \otimes \boldsymbol{n}$ on the surface, we use $\boldsymbol{B}_\parallel = B^{ij} \boldsymbol{g}_i \otimes \boldsymbol{g}_j$ to denote its tangential components and $\boldsymbol{B}_\perp = B^i_n \boldsymbol{g}_i \otimes \boldsymbol{n}$ to denote its cross components between tangential and normal directions.

To describe the spatial variation of the field, we introduce the covariant derivative of $\boldsymbol{a}(s^1,s^2,t)$ and $\boldsymbol{B}(s^1,s^2,t)$ as

$$\nabla_j a^i = (\partial_j \boldsymbol{a})\cdot \boldsymbol{g}^i, \tag{1}$$

$$\nabla_k B^{ij} = (\partial_k \boldsymbol{B}) : \boldsymbol{g}^i \otimes \boldsymbol{g}^j, \tag{2}$$

where ∇_j denotes the covariant derivative with respect to the surface coordinates.

With these notations in preparation, we define the gradient of the vector field $\boldsymbol{a}$ and the tensor field $\boldsymbol{B}$ as

$$\nabla \otimes \boldsymbol{a} = \boldsymbol{g}^i \otimes \partial_i \boldsymbol{a}, \tag{3}$$

$$\nabla \otimes \boldsymbol{B} = \boldsymbol{g}^i \otimes \partial_i \boldsymbol{B}. \tag{4}$$

The divergence of $\boldsymbol{a}$ and $\boldsymbol{B}$ reads

$$\mathrm{div}\,(\boldsymbol{a}) = \boldsymbol{g}^i \cdot \partial_i \boldsymbol{a}, \tag{5}$$

$$\mathrm{div}\,(\boldsymbol{B}) = \boldsymbol{g}^i \cdot \partial_i \boldsymbol{B}. \tag{6}$$

To describe the motion of the cortical flow, we introduce a velocity field $\boldsymbol{v}(s^1,s^2,t)$ on the surface,

$$\boldsymbol{v} = v^i \boldsymbol{g}_j + v_n \boldsymbol{n}. \tag{7}$$

The tangential components $\boldsymbol{v}_\parallel$ represent the in-plane flows, and the normal components $\boldsymbol{v}_\perp$ represent the deformation of the surface. With the flow field $\boldsymbol{v}$ defined, we can introduce the total time derivative $\mathrm{d}\boldsymbol{a}/\mathrm{d}t$ and $\mathrm{d}\boldsymbol{B}/\mathrm{d}t$ to describe the temporal variation of the vector field $\boldsymbol{a}$ and the tensor field $\boldsymbol{B}$,

$$\frac{\mathrm{d}\boldsymbol{a}}{\mathrm{d}t} = \partial_t \boldsymbol{a} + q^i \partial_i \boldsymbol{a}, \tag{8}$$

$$\frac{\mathrm{d}\boldsymbol{B}}{\mathrm{d}t} = \partial_t \boldsymbol{B} + q^i \partial_i \boldsymbol{B}, \tag{9}$$

where the components q^i of the coordinate flow $\boldsymbol{q} = q^i \boldsymbol{g}_i$ describe the motion of a surface point $\boldsymbol{X}$ at fixed coordinates s^i, relative to the in-plane center-of-mass velocity $\boldsymbol{v}_\parallel$ of that surface point. The velocity field $\boldsymbol{v}$ in Eq. (7) is related to the surface shape $\boldsymbol{X}$ via the equation

$$\boldsymbol{v} = \frac{\mathrm{d}\boldsymbol{X}}{\mathrm{d}t}. \tag{10}$$

Different choices of q^i lead to distinct coordinate representations of the surface. If $q^i = 0$, the surface coordinates s^i constitute the material coordinates and represent the Lagrangian representation. If $q^i = v^i$, the motion of the surface point $\boldsymbol{X}$ with fixed s^i only has a normal component, therefore leads to the Eulerian representation. The other choices of q^i are termed arbitrary-Lagrangian–Eulerian (ALE) representation.[64] For a more detailed explanation of the coordinate flow $\boldsymbol{q}$, we refer the readers to our work in Ref. [65]. The total time derivatives (also called the material derivatives) defined in Eqs. (8) and (9) represent the rate of change of a physical quantity as observed while moving with a fluid particle. It accounts for both local and convective changes in the field $\boldsymbol{a}$ and $\boldsymbol{B}$.

We next introduce the corotational time derivative of $\boldsymbol{a}$ and $\boldsymbol{B}$ as

$$\frac{\mathrm{D}\boldsymbol{a}}{\mathrm{D}t} = \frac{\mathrm{d}\boldsymbol{a}}{\mathrm{d}t} - \boldsymbol{\omega} \times \boldsymbol{a}, \tag{11}$$

$$\frac{\mathrm{D}\boldsymbol{B}}{\mathrm{D}t} = \frac{\mathrm{d}\boldsymbol{B}}{\mathrm{d}t} - \boldsymbol{\omega} \times_1 \boldsymbol{B} - \boldsymbol{\omega} \times_2 \boldsymbol{B}, \tag{12}$$

where $\boldsymbol{\omega} = \frac{1}{2}\nabla \times \boldsymbol{v}$ is the vorticity of the velocity field $\boldsymbol{v}$. The notations $\times_1$ and $\times_2$ in Eq. (12) represent cross products with the first and second members of the dyad forming $\boldsymbol{B}$, respectively. In covariant forms, Eq. (12) can be expressed as

$$\begin{aligned}\frac{\mathrm{D}B^{ij}}{\mathrm{D}t} = {} & \frac{\mathrm{d}B^{ij}}{\mathrm{d}t} + v_n C^j_k B^{ik} + v_n C^i_k B^{kj} \\ & + \left(\frac{1}{2}\epsilon^{lm}(\nabla_l v_m)\right)\left(\epsilon^{ik}B_k{}^j + \epsilon^j{}_k B^{ik}\right).\end{aligned} \tag{13}$$

The corotational time derivative defined in Eqs. (11) and (12) represents the material change of the field while excluding the contribution from rotation of the surface in which the vector/tensor is embedded.

2.3. Surface strain rate tensor

To characterize the in-plane deformation of the flow field $\boldsymbol{v}$, we introduce the strain rate tensor $\boldsymbol{S} = S^{ij}\boldsymbol{g}_i \times \boldsymbol{g}_j$, which is defined as the symmetric part of $\boldsymbol{g}_i \cdot \partial_j \boldsymbol{v}$. The components of $\boldsymbol{S}$ read

$$S_{ij} = \frac{1}{2}(\nabla_i v_j + \nabla_j v_i) + C_{ij} v_n. \tag{14}$$

We further split the symmetric tensor $S_{ij} = \tilde{S}_{ij} + S^{\mathrm{iso}}_{ij}$ into its traceless part

$$\tilde{S}_{ij} = S_{ij} - \frac{1}{2} S^k_k g_{ij}, \tag{15}$$

which describes the shear rate of the flow, and the isotropic part

$$S^{\mathrm{iso}}_{ij} = \frac{1}{2} S^k_k g_{ij}, \tag{16}$$

which describes the area change rate of the flow.

2.4. Surface nematic tensor

To describe the local orientational order of actin filaments, we introduce a second-rank tangent tensor $\boldsymbol{Q}(s^1,s^2,t)$ on the surface,

$$\boldsymbol{Q} = Q^{ij}\boldsymbol{g}_i \otimes \boldsymbol{g}_j, \tag{17}$$

with the symmetry $Q^{ij} = Q^{ji}$, and its trace $Q^k_k = 0$. It can be decomposed as

$$Q_{ij} = S_Q\left(p_i p_j - \frac{1}{2} g_{ij}\right), \tag{18}$$

where the normalized tangent vector $\boldsymbol{p} = p^i \boldsymbol{g}_i$ denotes the direction of the actin filaments. The scalar S_Q represents the degree of alignment, with $S_Q = 1$ indicating perfect alignment and $S_Q = 0$ indicating isotropic (no preferred direction).

2.5. Active stress regulators on the surface

Actin cortex is an out-of-equilibrium system driven by active stress regulators within the cortex, such as myosin motors, that are able to convert the chemical energy into mechanical stress. Gradients of the stresses create cortical flows that redistribute the stress regulators on the surface. We describe the active stress regulators with a surface concentration field $\rho(s^1, s^2, t)$, whose dynamics are governed by the equation

$$\partial_t \rho + q^i \partial_i \rho = -\mathrm{div}\,(\boldsymbol{v})\rho + D\Delta\rho - k(\rho - \rho_0). \tag{19}$$

The left side denotes the total time derivative of the concentration field ρ. On the right side, the first term describes the accumulation/reduction of concentration due to the local area compression ($\mathrm{div}\,(\boldsymbol{v}) < 0$)/dilation ($\mathrm{div}\,(\boldsymbol{v}) > 0$). In-plane diffusion of the stress regulators is captured by the Laplace–Beltrami operator $\Delta\rho = \nabla^i \nabla_i \rho$ in the second term with a diffusion constant D. The last term describes the turnover of stress regulators between the cortex and the cytoplasm, which results in a preferred concentration of the stress regulators ρ_0 and a turnover rate k.

Furthermore, we assume that the chemical reaction associated with stress generation proceeds with a rate r_p and the chemical potential difference $\Delta\mu$ is maintained constant in space and time.

2.6. Constitutive relation on the surface

In Ref. [12], the authors have laid out a framework to systematically derive the constitute relations of active nematic surfaces using the Onsager reciprocal relation. The idea relies on calculating the entropy production rate Θ, which is expressed as the product of a number of conjugate fluxes and forces. The constitutive law is then obtained by expressing the fluxes as a linear combination of the forces. The coupling coefficients have to obey symmetry/anti-symmetry rules imposed by the Onsager reciprocal relation according to the time reversal symmetry of the forces.[66,67] We refer the readers to Ref. [12] for the detailed calculation of the entropy production rate Θ. Here we directly provide the result

$$\Theta = \int \left(\boldsymbol{T}_\mathrm{d} : \boldsymbol{S} + \frac{\mathrm{D}\boldsymbol{Q}}{\mathrm{D}t} : \boldsymbol{H}_\mathrm{tan} + r_\mathrm{p}\Delta\mu \right) \mathrm{d}A, \tag{20}$$

where the fluxes and forces are listed in Table 1. For simplicity, contributions from the gradient of vorticity and chemical potentials in Eq. (20) are neglected.

Table 1. List of conjugate forces and fluxes for an active fluid nematic surface. The third column lists the time reversal signature of the force ϵ, with $\epsilon = +1$ indicating that the force is invariant under time reversal, $\epsilon = -1$ indicating that the force reverses its sign under time reversal.

Force	Flux	ϵ
Strain rate tensor $\boldsymbol{S}$	In-plane dissipative stress $\boldsymbol{T}_\mathrm{d}$	-1
Tangential part of the molecular field tensor $\boldsymbol{H}_\mathrm{tan}$	Corotational time derivative of nematic tensor $\mathrm{D}\boldsymbol{Q}/\mathrm{D}t$	$+1$
Chemical energy difference $\Delta\mu$	Fuel consumption rate r_p	$+1$

The constitutive laws associated with the entropy production rate in Eq. (20) are listed below:

$$\frac{\mathrm{D}\boldsymbol{Q}}{\mathrm{D}t} = \beta_1 \tilde{\boldsymbol{S}} + \frac{1}{\beta_2}\boldsymbol{H}_\mathrm{tan} + \zeta\Delta\mu f(\rho)\boldsymbol{Q}, \tag{21}$$

$$\boldsymbol{T}_\mathrm{d} = 2\eta_\mathrm{s}\tilde{\boldsymbol{S}} + 2\eta_\mathrm{b}\boldsymbol{S}^\mathrm{iso} - \beta_1 \boldsymbol{H}_\mathrm{tan} + \xi\Delta\mu f(\rho)\boldsymbol{Q}, \tag{22}$$

$$r_\mathrm{p} = \zeta f(\rho)\boldsymbol{Q} : \boldsymbol{H}_\mathrm{tan} - \xi f(\rho)\boldsymbol{Q} : \boldsymbol{S} + \Lambda\Delta\mu. \tag{23}$$

Equation (21) defines the dynamics of the nematic tensor $\boldsymbol{Q}$. The first term represents the flow-alignment coupling, where the filaments generally tend to align along the direction of stretching, resulting in $\beta_1 > 0$.[58] The second term describes the relaxation of the filament orientation to minimize elastic energy F_Q, which will be discussed in Subsection 2.7, with rotational viscosity β_2. The molecular field $\boldsymbol{H}$ is obtained by varying the elastic energy F_Q with respect to the nematic tensor $\boldsymbol{Q}$, which yields $\boldsymbol{H} = -\delta F_Q/\delta\boldsymbol{Q}$, whose tangential components are denoted by $\boldsymbol{H}_\mathrm{tan}$. The final term in Eq. (21) represents active alignment induced by chemical reactions, characterized by the alignment strength ζ. The physical origin of this term can be understood as follows: When two motor proteins are positioned between two filaments at a tilt relative to their orientation, the forces they generate have parallel and perpendicular components with respect to the direction of the filament. The parallel component induces filament sliding, while the perpendicular component acts as a torque, aligning the filaments. However, this contribution has often been overlooked in previous studies on flat surfaces.

Equation (22) gives the expression for the dissipative stress $\boldsymbol{T}_\mathrm{d}$. The first two terms represent the viscous stresses associated with shear (η_s) and area change (η_b), respectively. The third term represents the cross-coupling between the flux $\boldsymbol{T}_\mathrm{d}$ and the force $\boldsymbol{H}_\mathrm{tan}$. The minus sign in front of β_1 is due to the opposite time-reversal symmetry between $\boldsymbol{T}_\mathrm{d}$ and $\mathrm{D}\boldsymbol{Q}/\mathrm{D}t$. The last term in Eq. (22) represents the active stress produced by stress regulators that could be contractile ($\xi > 0$) or extensive ($\xi < 0$). For the actin cortex, active stress is typically considered contractile.[68–71] Note that the nematic tensor $\boldsymbol{Q}$ in the last term indicates that when the actin filaments are in an isotropic phase $\boldsymbol{Q} = 0$, the active stress vanishes. Furthermore, this suggests that the active stress is anisotropic, which means that the stresses differ in their signs between the directions parallel and perpendicular to the actin filaments. In general, an isotropic active stress (proportional to the metric tensor $\boldsymbol{G}$) is also allowed. In this study, we focus on the effect of anisotropic stress and neglect isotropic active stress.

Equation (23) gives the fuel consumption rate r_p. The first term indicates that cross coupling between the flux r_p and the force $\boldsymbol{H}_\mathrm{tan}$ and the coupling constant ζ is symmetric because $\Delta\mu$ and $\boldsymbol{H}_\mathrm{tan}$ have the same time reversal signature. The second term represents the coupling between r_p and $\boldsymbol{S}$, while the coupling constant ξ is antisymmetric due to the opposite time reversal signature of $\Delta\mu$ and $\boldsymbol{S}$.

The function $f(\rho)$ in Eqs. (21), (22), (23) represents the regulation strength of the active stress and the active alignment tuned by the concentration field ρ of the stress regulators. We use a saturating Hill function

$$f(\rho) = \frac{\rho^m}{\rho^m + \rho_s^m} \tag{24}$$

to describe the regulation dependence on ρ and use $m = 2$ in this paper. The density dependence simply indicates that a higher number of motor proteins generates greater stresses in both the parallel and perpendicular directions relative to the orientation of the filament.

2.7. Elastic energy of the surface

The elasticity of the cortical surface has two origins, one from the curvature of the surface itself, the other from the orientational order of actin filaments embedded in the surface. The former is described by the Helfrich energy

$$F_{\mathrm{H}} = \int f_{\mathrm{H}} \mathrm{d}A = \int_{\Omega} \left[\sigma + \frac{\kappa}{2} \left(C_k^k \right)^2 \right] \mathrm{d}A, \tag{25}$$

where σ denotes the surface tension and κ denotes the bending rigidity. We do not include the Gaussian curvature term which only contributes a constant if no topological change of the surface is considered due to the famous Gauss–Bonnet theorem.[72] In addition, we introduce a Lagrangian multiplier p, which can be interpreted as the pressure difference between inside and outside of the cell, to impose a conserved volume V of the cell,

$$F_{\mathrm{p}} = -pV. \tag{26}$$

The Helfrich model has been widely used to discuss cellular deformations.[73–75] The value of model parameters can be determined by either experiment or field theory.[76] Moreover, its elastic properties can be adjusted by the interaction with the nanoparticles.[77,78] Besides the cellular morphology, the mathematical aspect of this model is also attractive, leading to many intriguing results. In the axisymmetric case, some analytical solutions[79] and a first integral[80] have been found.

The elastic energy associated with the nematic tensor $\boldsymbol{Q}$ reads

$$F_Q = \int f_Q \mathrm{d}A, \tag{27}$$

where the energy density f_Q is given by the following expression:

$$f_Q = \frac{K}{2} \left[A_1 \boldsymbol{Q} : \boldsymbol{Q} + \frac{A_2}{2} (\boldsymbol{Q} : \boldsymbol{Q})^2 + L_{\mathrm{n}}^2 (\nabla \boldsymbol{Q} : \nabla \boldsymbol{Q}) \right]. \tag{28}$$

In covariant forms, it can be written as

$$\begin{aligned} f_Q = {} & \frac{KA_1}{2} Q^{ij} Q_{ij} + \frac{KA_2}{4} \left(Q^{ij} Q_{ij} \right)^2 \\ & + \frac{KL_{\mathrm{n}}^2}{2} \left(\nabla_k Q_{ij} \right) \left(\nabla^k Q^{ij} \right) \\ & + \frac{KL_{\mathrm{n}}^2}{2} \left(Q^{lj} Q_j^k C_l^p C_{pk} + Q^{il} Q_i^j C_l^k C_{kj} \right). \end{aligned} \tag{29}$$

The first line in Eq. (29) is known as the phase energy. The constant $A_2 > 0$ is required to ensure that the free energy has a lower bound. The constant $A_1 > 0$ indicates an isotropic phase ($S_Q = 0$) is preferred in equilibrium and $A_1 < 0$ indicates a nematic phase ($S_Q > 0$). The second and third lines arise from the spatial variation of the nematic tensor $\boldsymbol{Q}$. They together can be seen as a simplified generalization of the well-known Landau–de Gennes energy in liquid crystals on curved surfaces.[81] We stress that the third line introduces a coupling between the nematic tensor $\boldsymbol{Q}$ and the curvature tensor $\boldsymbol{C}$, therefore the shape of the surface can influence the actin orientation, and vice versa.

Given the free energy density f_Q in Eq. (29), the tensor $\boldsymbol{H}_{\mathrm{tan}}$, which is the conjugate force to the flux $\mathrm{D}\boldsymbol{Q}/\mathrm{D}t$ in the entropy production rate (Eq. (20)), can be expressed as

$$\begin{aligned} \boldsymbol{H}_{\mathrm{tan}} = {} & \left(-KA_1 - KA_2 \left(Q^{lm} Q_{lm} \right) \right) \boldsymbol{Q} + KL_{\mathrm{n}}^2 \\ & \times \left[\nabla_k \nabla^k Q^{ij} - Q^{il} C_l^k C_k^j - Q^{jl} C_l^k C_k^i \right] \boldsymbol{g}_i \boldsymbol{g}_j \\ & + KL_{\mathrm{n}}^2 Q^{lm} C_{lm} C_k^k \boldsymbol{G}. \end{aligned} \tag{30}$$

The last line in Eq. (30) is to ensure $\boldsymbol{H}_{\mathrm{tan}}$ is a traceless tensor.

The total elastic energy F_{E} is a sum of the three types of elastic energies mentioned above

$$F_{\mathrm{E}} = F_{\mathrm{H}} + F_Q + F_{\mathrm{p}}. \tag{31}$$

2.8. Force balance equation

To describe the surface dynamics as a result of the mechanical stresses $\boldsymbol{T}$ within it and the external force $\boldsymbol{T}_{\mathrm{ext}}$ acting on it, in the limit of small Reynolds number, we can neglect the inertial term and write the force balance equation as

$$\mathrm{div}\left(\boldsymbol{T}_{\mathrm{tot}} \right) = -\boldsymbol{f}_{\mathrm{ext}}, \tag{32}$$

where the total stress $\boldsymbol{T}_{\mathrm{tot}}$ is composed of three parts

$$\boldsymbol{T}_{\mathrm{tot}} = \boldsymbol{T}_{\mathrm{d}} + \boldsymbol{T}_{\mathrm{e}} + \boldsymbol{H}_{\mathrm{tan}} \cdot \boldsymbol{Q} - \boldsymbol{Q} \cdot \boldsymbol{H}_{\mathrm{tan}}. \tag{33}$$

The first term in Eq. (33) denotes the dissipative stress which is given by Eq. (22). The equilibrium stress $\boldsymbol{T}_{\mathrm{e}}$ in Eq. (33) is derived from the Helfrich elastic energy (25) and the nematic elastic energy (27).[12] The contribution to $\boldsymbol{T}_{\mathrm{e}}$ from the Helfrich energy F_{H} has its tangential components

$$t_{\mathrm{E}}^{ij} = f_{\mathrm{H}} g^{ij} - K^{ik} C_k^j, \tag{34}$$

and normal components

$$t_{\mathrm{E,n}}^{i} = \nabla_j K^{ji}, \tag{35}$$

where $K^{ij} = \partial f_{\rm H}/\partial C_{ij}$ denotes the passive bending moment tensor. The contribution to $\boldsymbol{T}_{\rm e}$ from the nematic elastic energy F_Q has its tangential components

$$t_Q^{ij} = f_Q g_{ij} - \boldsymbol{\Pi}^i : \partial^j \boldsymbol{Q}, \tag{36}$$

and normal components

$$t_{Q,\rm n}^i = -\epsilon^i{}_j (\boldsymbol{H}_{\rm tan} \times_1 \boldsymbol{Q} + \boldsymbol{H}_{\rm tan} \times_1 \boldsymbol{Q}) \cdot \boldsymbol{g}^j, \tag{37}$$

where $\boldsymbol{\Pi}^i = \boldsymbol{g}^i \cdot \boldsymbol{\Pi}$ and $\boldsymbol{\Pi} = \partial f_Q/\partial(\nabla \otimes \boldsymbol{Q})$. The last term in Eq. (33) denotes the antisymmetric tensor arising from rotational invariance of the free energy f_Q.

Additionally, we introduce an effective frictional force acting on the surface, which describes the dissipative interaction between the surface flow and the ambient environment. This is captured by the tangential components of the external force density

$$f_{\rm ext}^i = -\Gamma v^i. \tag{38}$$

The pressure energy in Eq. (26) leads to a normal component of the external force density

$$f_{\rm ext,n} = p. \tag{39}$$

So far, we have introduced the model for the active nematic surface to describe the active deformation of actin cortex. One can solve the force balance equation (32), the dynamic equations for the nematic tensor $\boldsymbol{Q}$ (21) and the concentration field ρ (19) to obtain the dynamic evolution of the shape $\boldsymbol{X}$, the cortical flow $\boldsymbol{v}$, the nematic tensor $\boldsymbol{Q}$, and the concentration of stress regulators ρ.

3. Linearized axisymmetric surface dynamics

The general dynamic equations (19), (21), (32) form a set of coupled, nonlinear equations governing the surface shape $\boldsymbol{X}$, the cortical flow $\boldsymbol{v}$, the nematic tensor $\boldsymbol{Q}$, and the concentration field ρ. Solving these equations numerically is highly challenging. To simplify the analysis, we impose axisymmetry and linearize the equations around a steady state with a spherical surface. The resulting linearized equations are analytically tractable and provide valuable insights into the conditions required for self-organized cell division.

3.1. Field variables on an axisymmetric surface

An axisymmetric surface can be parameterized as

$$\boldsymbol{X}(u,\phi,t) = \{r(u,t)\cos(\phi), r(u,t)\sin(\phi), z(u,t)\}. \tag{40}$$

We introduce a dimensionless coordinate $u \in [0,1]$ to specify the meridional position on the surface, where $u = 0$ and $u = 1$ correspond to the north and south poles, respectively (Fig. 1(a)).

We also introduce two auxiliary functions $\psi(u,t)$ and $h(u,t)$ that satisfy the geometric relations

$$r' = h\cos\psi, \tag{41}$$

$$z' = -h\sin\psi. \tag{42}$$

Hereafter, we use prime to denote the derivative with respect to u. The function $\psi(u,t)$ represents the angle spanned between the tangential direction along the u-coordinate and $h(u,t)$ is related to the arclength $s(u,t)$ via the equation $s' = h$. With the help of the two functions, the metric tensor g_{ij} and curvature tensor C_{ij} read

$$g_{ij} = \begin{bmatrix} h^2 & 0 \\ 0 & r^2 \end{bmatrix}, \tag{43}$$

$$C_{ij} = \begin{bmatrix} h\psi' & 0 \\ 0 & r\sin\psi \end{bmatrix}. \tag{44}$$

The two principal curvatures can be simplified as

$$C_\phi^\phi = \frac{\sin\psi}{r}, \tag{45}$$

$$C_u^u = \frac{\psi'}{h}. \tag{46}$$

The axisymmetric velocity field $\boldsymbol{v}$ reads

$$\boldsymbol{v} = v_u(u,t)\boldsymbol{e}_u + v_\phi(u,t)\boldsymbol{e}_\phi + v_n(u,t)\boldsymbol{n}, \tag{47}$$

where $\boldsymbol{e}_u = \partial_u \boldsymbol{X}/h$ and $\boldsymbol{e}_\phi = \partial_\phi \boldsymbol{X}/r$ are normalized basis vectors that span the tangential space of the surface. The symmetric and traceless nematic tensor $\boldsymbol{Q}$ with axisymmetry can be expressed as

$$\begin{aligned}\boldsymbol{Q}(u,t) \;=\; & Q_{\rm a}(u,t)(\boldsymbol{e}_u \otimes \boldsymbol{e}_u - \boldsymbol{e}_\phi \otimes \boldsymbol{e}_\phi) \\ & + Q_{\rm b}(u,t)(\boldsymbol{e}_\phi \otimes \boldsymbol{e}_u + \boldsymbol{e}_u \otimes \boldsymbol{e}_\phi).\end{aligned} \tag{48}$$

Last, the concentration field $\rho = \rho(u,t)$ only depends on the meridional coordinate u.

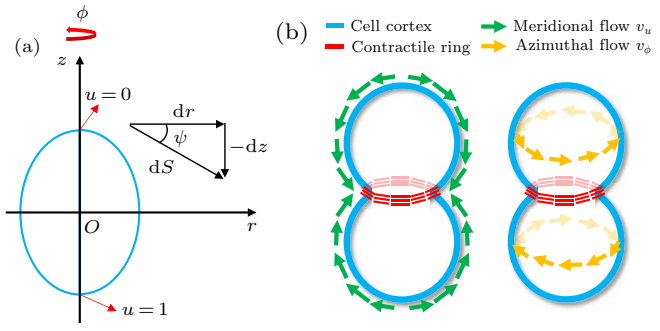


Fig. 1. (a) Geometric representation of an axisymmetric surface with spherical topology. The dimensionless coordinate $u \in [0,1]$ is to denote the meridional position along the surface profile $\{r(u,t), z(u,t)\}$, with $u = 0$ and $u = 1$ corresponding to the north and south poles of the surface, respectively. (b) The sketch of the deformation and cortical flows induced by nematic instability $l = 2$. The shape coefficient $\delta R^{(2)} > 0$ indicates that the surface is squeezed at the equator (blue line). The concentration coefficient $\delta\rho^{(2)} < 0$ indicates that stress regulators are concentrated at the equator (red line). The velocity coefficient $\delta v_u^{(2)} < 0$ indicates that the meridional flows go from the poles to the equator (green arrows on the left), $\delta v_\phi^{(2)} \neq 0$ indicates that the azimuthal flows go in opposite directions in the two hemispheres (orange arrows on the right).

3.2. A steady state solution

The system of Eqs. (19), (21), and (32) has a steady state where the shape of the surface is spherical

$$r^*(u) = R_0 \sin(u\pi), \tag{49}$$

$$z^*(u) = R_0 \cos(u\pi), \tag{50}$$

with a radius of R_0. The cortical flow is immobile, i.e., $\boldsymbol{v}^* = \boldsymbol{0}$, and the orientational order of actin filaments is isotropic, i.e., $\boldsymbol{Q}^* = \boldsymbol{0}$. Stress regulators are uniformly distributed on the sphere with $\rho^* = \rho_0$. The pressure difference $p^* = 2\sigma/R_0$. This steady state always exists regardless of the model parameters. However, the stability of the steady state may vary with parameters. In this section, we make a small perturbation to the steady state, and investigate how the stability of the steady state depends on model parameters.

3.3. Linearized equations

Following Refs. [61,62], we make a perturbation of the field variables around the steady state,

$$\rho = \rho^* + \delta\rho(u,t), \tag{51}$$

$$r = r^* + \delta R(u,t)\sin(u\pi), \tag{52}$$

$$z = z^* + \delta R(u,t)\cos(u\pi), \tag{53}$$

$$\boldsymbol{v} = \boldsymbol{v}^* + \delta\boldsymbol{v}(u,t), \tag{54}$$

$$\boldsymbol{Q} = \boldsymbol{Q}^* + \delta\boldsymbol{Q}(u,t). \tag{55}$$

We then substitute Eqs. (51)–(55) into Eqs. (19), (21), (32), and expand the equations up to first order of the perturbations, thus obtaining 6 linearized equations, including 3 force balance equations, 2 dynamic equations about the nematic tensor, and 1 dynamic equation about the concentration field. We then expand the perturbation functions as

$$\delta\rho(u,t) = \sum_{l=1}^{\infty} \delta\rho^{(l)}(t) Y_{l0}(u\pi), \tag{56}$$

$$\delta R(u,t) = \sum_{l=1}^{\infty} \delta R^{(l)}(t) Y_{l0}(u\pi), \tag{57}$$

$$\delta\boldsymbol{v}(u,t) = \sum_{l=1}^{\infty} \delta v_u^{(l)}(t)\boldsymbol{\Psi}_{l0}(u\pi) + \delta v_\phi^{(l)}(t)\boldsymbol{\Phi}_{l0}(u\pi), \tag{58}$$

$$\delta\boldsymbol{Q}(u,t) = \sum_{l=2}^{\infty} \delta Q_{\mathrm{a}}^{(l)}(t)\bar{\boldsymbol{\Psi}}_{l0}(u\pi) + \delta Q_{\mathrm{b}}^{(l)}(t)\bar{\boldsymbol{\Phi}}_{l0}(u\pi), \tag{59}$$

where Y_{lm}, $\boldsymbol{\Psi}_{lm}/\boldsymbol{\Phi}_{lm}$, $\bar{\boldsymbol{\Psi}}_{lm}/\bar{\boldsymbol{\Phi}}_{lm}$ are scalar, vector and tensor spherical harmonic functions, respectively, whose definitions are provided in Appendix A. As we restrict our study to the axisymmetric case, we only choose spherical harmonic functions with $m = 0$, whose values are independent of the azimuthal angle ϕ. We do not include $l = 0$ mode in the expansion because volume conservation implies that $\delta R^{(0)} = 0$. The coefficient $\delta\rho^{(0)}$ implies a homogeneous change of the concentration which only leads to relaxation of the concentration to its preferred value ρ_0, therefore, it is always stable. The modes $\delta R^{(l)}$ with $l \geq 1$ do not, to linear order, affect the enclosed volume. Consequently, there are no first-order contributions to pressure perturbations $\delta p^{(l)}$ for $l \geq 1$.

We stress that different l-modes represent distinct trends for the dynamics. For instance, the $l = 1$ mode represents a polarization mode that breaks the up-down symmetry. The $l = 2$ mode represents a nematic mode that is particularly relevant for cell division in four aspects (see Fig. 1(b)): (1) the surface shape is squeezed at the equator ($\delta R^{(2)} > 0$); (2) the cortical flow goes from the poles to the equator ($\delta v_u^{(2)} < 0$); (3) the stress regulators are concentrated at the equator ($\delta\rho^{(2)} < 0$); (4) actin filaments at the equator are aligned in the azimuthal direction ($\delta Q_{\mathrm{a}}^{(2)} < 0$). Therefore, finding parameter regimes where $l = 2$ is the only unstable mode is particularly relevant to achieving robust cell division against small perturbations.

Furthermore, the coefficient $\delta v_\phi^{(2)} \neq 0$ indicates a chiral flow such that flows in the two hemispheres are rotating along azimuthal directions but in opposite trends. The coefficient $\delta Q_{\mathrm{b}}^{(2)} \neq 0$ implies a chiral alignment of the actin filaments whose direction has a tilted angle relative to the azimuthal direction.

3.4. Jacobian matrix and stability

We substitute Eqs. (56)–(59) into the 6 linearized equations. It turns out that the different l-modes are decoupled and for each l we obtain 6 equations about the six coefficients $\{\delta\rho^{(l)}, \delta R^{(l)}, \delta v_u^{(l)}, \delta v_\phi^{(l)}, \delta Q_{\mathrm{a}}^{(l)}, \delta Q_{\mathrm{b}}^{(l)}\}$. Using the two force balance equations in the tangent directions, we can express $\delta v_u^{(l)}, \delta v_\phi^{(l)}$ as a function of the other 4 variables. The rest four equations can be finally reduced to the form

$$\frac{\mathrm{d}}{\mathrm{d}t}(\delta\boldsymbol{\Omega}^{(l)}) = \boldsymbol{J}^{(l)}\delta\boldsymbol{\Omega}^{(l)}, \tag{60}$$

where $\delta\boldsymbol{\Omega}^{(l)} = (\delta R^{(l)}, \delta\rho^{(l)}, \delta Q_{\mathrm{a}}^{(l)}, \delta Q_{\mathrm{b}}^{(l)})^{\mathrm{T}}$ denotes the column vector of the perturbation coefficients, and $\boldsymbol{J}^{(l)}$ is the 4×4 Jacobian matrix. If one of the eigenvalues of the Jacobian matrix $\boldsymbol{J}^{(l)}$ has a positive real part, the l-mode will become unstable, thus growing over time. We use the largest real part of the eigenvalues $\mathrm{Re}\lambda_i$ to define the growth rate of the mode.

3.5. Choices of parameters

Our model includes multiple parameters whose combination can make up 5 length scales $R_0, L_{\mathrm{h}} = \sqrt{\eta_{\mathrm{b}}/\Gamma}$, $L_{\mathrm{H}} = \sqrt{\kappa/\sigma}$, $L_{\mathrm{K}} = \sqrt{\kappa/K}$, L_{n}. We use the cell size R_0 as the unit length to rescale the other lengths. The ratio of the cell size R_0 to the hydrodynamic length L_{h} tells whether the internal viscosity or the external friction dominates the system's dissipation. If $R_0 \ll L_{\mathrm{h}}$, the internal viscosity overwhelms the external friction. In contrast, $R_0 \gg L_{\mathrm{h}}$ means that the cortex

flow is strongly affected by the interaction with its surroundings. Later we will see that this ratio is important for inducing nematic ($l = 2$) instability. For simplicity, we fix all the other length scales the same as the cell size R_0, including L_H, L_K, L_n.

The combination of parameters can make up 4 time scales $\tau_D = R_0^2/D$, $\tau_\xi = \eta_b/(\xi\Delta\mu)$, $\tau_\zeta = 1/(\zeta\Delta\mu)$, $\tau_k = 1/k$. We use the diffusion time τ_D as the unit time to rescale other time scales. The velocity scale is defined as $v_c = R_0/\tau_D$. The ratio of diffusion time τ_D to convective time τ_ξ determines a dimensionless parameter $Pe = \tau_D/\tau_\xi = \xi\Delta\mu R_0^2/(\eta_b D)$, the Péclet number, which measures the strength of the active stress that induces convective flows relative to diffusive flows. The ratio $\tau_D/\tau_\zeta = \zeta\Delta\mu R_0^2/D$ measures the strength of the active alignment of actin filaments. Later, we will vary these two dimensionless parameters and fix the ratio $\tau_D/\tau_k = 1$.

The flow-alignment coupling constant β_1 is a dimensionless parameter that also plays an important role in generating nematic instability. We will vary β_1 later to show its effect. The other dimensionless parameters are given as $\eta_s/\eta_b = 1$, $\beta_2/\eta_b = 1$, $A_1 = 1$, $\rho_s/\rho_0 = 0.5$. To summarize, one can refer to Table 2 for more details on model parameters.

Table 2. The meaning and value of model parameter. The basic length scale is chosen as the initial radius of the cell R_0, and the basic time scale is chosen as ${R_0}^2/D$, where D is the diffusion coefficient of motors. The concentration is scaled by the equilibrium motor concentration ρ_0. The energy is scaled by the bending rigidity, κ, of the Helfrich model.

Parameter	Meaning	Value	Unit
σ	surface tension of fluid	1	$\kappa/{R_0}^2$
K	bending modulus of Landau–de Gennes model	1	$\kappa/{R_0}^2$
A_1	linear phase energy of nematic matter	1	dimensionless
A_2	quadratic phase energy of nematic matter	1	dimensionless
L_n	characteristic length of nematic alignment	1	R_0
η_b	bulk viscosity	1	κ/D
η_s	shear viscosity	1	κ/D
Γ	external friction	variable	$\kappa/(R_0^2 D)$
β_1	flow-alignment coupling	variable	dimensionless
β_2	rotational viscosity	1	$K{R_0}^2/D$
ζ	active alignment	variable	$D/(R_0^2\Delta\mu)$
ξ	nematic active stress	variable	$\kappa/(R_0^2\Delta\mu)$
v_c	characteristic velocity	1	D/R_0
k	motor turnover rate	1	$D/{R_0}^2$
ρ_s	saturated motor concentration	0.5	ρ_0
L_h	hydrodynamic length	variable	R_0
L_H	characteristic length of the Helfrich model	1	R_0
L_K	characteristic cortical bending length	1	R_0
Pe	Péclet number	variable	dimensionless
$\zeta\Delta\mu R_0^2/D$	measurement of active alignment	variable	dimensionless

4. Results

4.1. Instability induced by active contractility and active alignment

We first present a simple example of the linear stability analysis to demonstrate how the active contractility strength Pe influence the stability of different modes. In Fig. 2, we show the growth rates for the first five modes under different Pe. The active alignment strength is fixed at $\zeta\Delta\mu = 20/\tau_D$. Note that even in the absence of active stress (i.e., $Pe = 0$), the $l = 2, 3$ instabilities can be promoted, because the active alignment allows excitation of the nematic tensor $\boldsymbol{Q}$, which leads to nonzero $-\beta_1 \boldsymbol{H}_{tan}$ in the dissipative stress $\boldsymbol{T}_d$ in Eq. (22) that deforms the surfaces. If the contractility is within the range of $Pe \in [15, 70]$ (e.g., see $Pe = 35$ line in Fig. 2), only the $l = 2$ mode is promoted. However, when the active contractility increases above $Pe = 70$, all the five modes become stable. It seems strange that a 'stronger' contractility is unable to induce instability. We will show later that this results from the fact that a large and positive Pe tends to inhibit the excitation of the nematic tensor $\boldsymbol{Q}$.

Note that the growth rate for $l = 1$ mode is always zero (Fig. 2). This is because $l = 1$ mode represents a polarization mode that breaks the nematic symmetry. The nematic active stress (proportional to $\boldsymbol{Q}$) used in our model cannot give a polarized mode. However, with an isotropic active stress, the polarization mode ($l = 1$) can be promoted, which has been studied in Ref. [82].

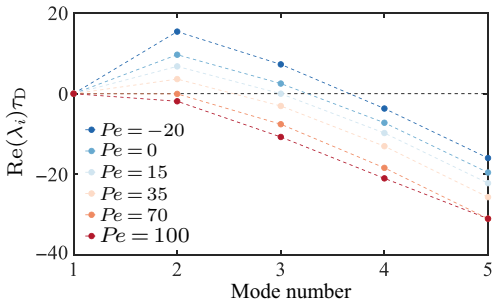


Fig. 2. The mode growth rates under different Péclet numbers. The growth rate is defined as the largest real part of the eigenvalues of the Jacobian matrix $\boldsymbol{J}^{(l)}$. The other key dimensionless parameters are set to $\zeta\Delta\mu R_0^2/D = 20, \beta_1 = 1, R_0/L_h = 1$.

In addition to the active contractility, we stress that active

alignment is also important in generating instabilities. To see that, we set $\zeta\Delta\mu = 0$ and keep all the other parameters the same as in Fig. 2, and show the growth rates for each mode in Fig. 3. All the unstable modes in Fig. 2 become stable, regardless of how strong the active contractility Pe is.

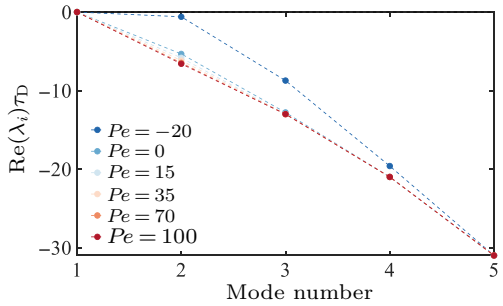


Fig. 3. The mode growth rates under different Péclet numbers ($\zeta\Delta\mu R_0^2/D = 0$). The other key dimensionless parameters are given by $\beta_1 = 1$, $R_0/L_\mathrm{h} = 1$.

4.2. Time evolution of the linearized dynamics

We then demonstrate the linearized dynamics for the perturbations with $Pe = 35$ such that only $l = 2$ mode is unstable. We start with an initial condition $\delta\boldsymbol{\Omega}^{(l)}(t=0) = (0,0,-0.01,-0.01)^\mathrm{T}$, which implies that actin filaments are slightly aligned in the azimuthal direction with weak chirality. We solve Eq. (60) to get the time evolution of the perturbations $\delta\boldsymbol{\Omega}^{(l)}(t)$. The velocity perturbations $\delta v_u^{(l)}(t)$ and $\delta v_\phi^{(l)}(t)$ are derived from the linearized force balance equations in the tangential directions. We show the time evolution of the perturbations for $l = 2$ in Fig. 4(a). The tiny initial perturbations in the nematic tensor $\delta Q_\mathrm{a}^{(2)}$ and $\delta Q_\mathrm{b}^{(2)}$ induce a nonzero $\delta v_u^{(2)}$ and $\delta v_\phi^{(2)}$. As the time evolves, all the perturbations grow over time except for $\delta v_\phi^{(2)}$ and $\delta Q_\mathrm{b}^{(2)}$. This indicates that the chirality finally disappears. The perturbations $\delta R^{(2)} > 0$ and $\delta Q_\mathrm{a}^{(2)} < 0$ at large t indicate a squeezed cell at the equator and alignment of actin filaments in the azimuthal direction, consistent with observations of cell division. However, $\delta v_u^{(2)} > 0$ and $\delta\rho^{(2)} > 0$ indicate cortical flows from the equator to the poles and more motors at the poles than at the equator, inconsistent with observations during cell division. We stress that if the initial perturbation reverses its sign, the final perturbation will also reverse its sign. Therefore, the linearized dynamics always predicts two consistent and two inconsistent observations with cell division, regardless of the initial conditions. As for the $l = 3$ or higher modes, all the perturbations decay over time.

When the active stress is extensile (i.e., $Pe < 0$), the linearized dynamics give rise to chiral flow, characterized by $\delta v_\phi^2 \neq 0$ and $\delta Q_\mathrm{b}^{(2)} \neq 0$, as illustrated in Fig. 4(b). In Subsection 4.1, we show that this phenomenon arises from the fact that extensile stress promotes the growth of $\delta Q_\mathrm{b}^{(2)}$ (see Eq. (62)), leading to a chiral alignment of actin filaments. This alignment, in turn, induces chiral flows, where cortical flows occur in the azimuthal direction and exhibit opposite trends in the two hemispheres.

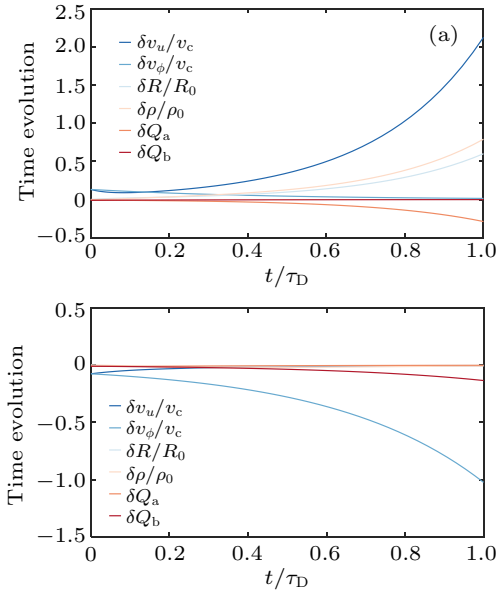


Fig. 4. Time evolution of the linearized equations for only $l = 2$ unstable mode. (a) The perturbations $\delta v_u, \delta R, \delta\rho, \delta Q_\mathrm{a}$ grow over time, which represent a squeezed sphere at the equator and actin filaments aligned in the azimuthal direction, cortical flows going from the equator to the poles and more motors at the poles than at the equator. (b) The perturbations δv_ϕ and δQ_b grow over time, which represent a chiral flow with counter-rotating azimuthal flows in the two hemispheres. The key dimensionless parameters are set as $Pe = 35$, $\zeta\Delta\mu R_0^2/D = 20$, $\beta_1 = 1$, $R_0/L_\mathrm{h} = 1$ in (a), $Pe = -30$, $\zeta\Delta\mu R_0^2/D = 0$, $\beta_1 = 1$, $R_0/L_\mathrm{h} = 1$ in (b).

4.3. Stability diagram of the linearized dynamics

To systematically investigate the dependence of the stability of different modes on model parameters, we choose four important dimensionless parameters, Pe, $\zeta\Delta\mu R_0^2/D$, R_0/L_h and β_1, and construct the stability diagram as a function of pairs from $\{Pe, R_0/L_\mathrm{h}, \beta_1\}$ with varied active alignment strength $\zeta\Delta\mu R_0^2/D$. The results are displayed in Figs. 5–7, where the parameter space is divided into the stable region (white) and the unstable region (gray).

Firstly, we fix the flow-alignment coupling $\beta_1 = 1$ and scan the parameters in the range $Pe \in [-30, 30], R_0/L_\mathrm{h} \in [0, 5]$ with varied $\zeta\Delta\mu R_0^2/D$. When the system displays no active alignment (Fig. 5(a)) or week alignment (Fig. 5(b)), a contractile stress ($Pe > 0$) cannot lead to the instability no matter how strong it is. However, one may find that there is still an unstable region of negative Pe, i.e., extensile stress. As the active alignment grows larger, the $l = 2$ mode at the $Pe > 0$ region begins to be motivated, especially in the region with larger R_0/L_h. Thus, one witnesses a boundary curve (red lines) with positive slopes in Figs. 5(c) and 5(d). When horizontally crossing the boundary curve from left to right, the system goes from stable to unstable. It indicates that with the same contractility, a large cell can divide while a small cell cannot. When vertically crossing the the boundary curve from down to up in Figs. 5(c) and 5(d), the system goes from unstable to stable. It

indicates that for a fixed cell size, too large contractility prevents the motivation of the $l = 2$ mode. As for strong active alignment, the $l = 3$ mode (orange lines in Figs. 5(c) and 5(d)) emerges following the $l = 2$ mode, which also becomes more significant with the increase in active alignment. The region between the $l = 2$ boundary curve (red) and $l = 3$ boundary curve (red) indicates a region with only $l = 2$ unstable mode.

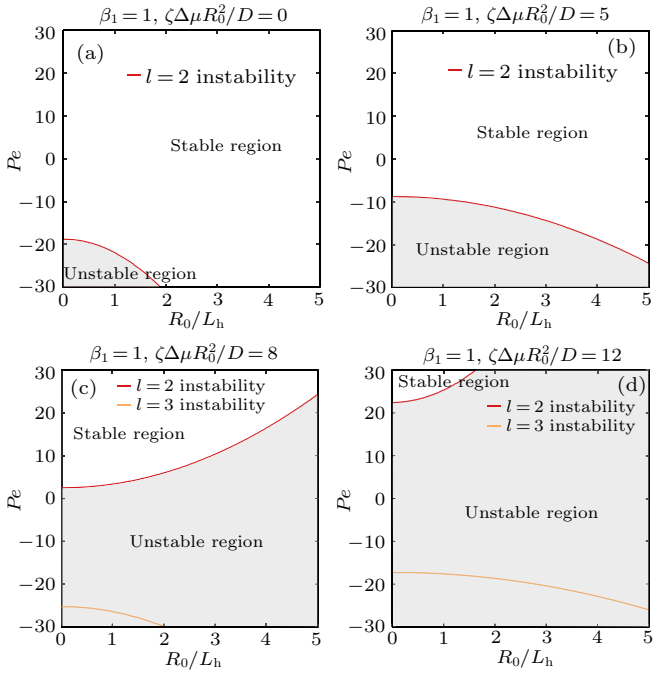


Fig. 5. The Pe–R_0/L_h mode stability diagram.

Secondly, we fix the cell size $R_0 = L_h$ and scan the parameters in the range $Pe \in [-30, 30], \beta_1 \in [0, 10]$. Likewise, the $l = 2$ instability induced by a contractile stress ($Pe > 0$) does not appear until the active alignment gets large enough. (see Figs. 6(a) and 6(b)). As the active alignment grows, more unstable modes can be activated (see Figs. 6(c) and 6(d)). When vertically crossing the boundary curve (red line) from down to up in Figs. 6(c) and 6(d), we find a similar phenomenon that too strong contractility prevents the $l = 2$ mode from going unstable. In contrast, an extensile stress can indeed promote the $l = 2$ mode. Moreover, when horizontally crossing the boundary line (red) from left to right in Figs. 6(c) and 6(d), one reveals that under very strong flow-alignment coupling, neither contractile nor extensile stress is favorable for the mode instabilities.

Thirdly, we investigate the stability of a cell with a fixed contractility $Pe = 20$, and scan the parameters in the range $R_0/L_h \in [0, 5], \beta_1 \in [0, 10]$ (Fig. 7). Generally, we have reproduced our observation in Figs. 5 and 6. When the cortex is driven by contractile stress, with a fixed flow-alignment strength β_1, a larger cell can divide while a smaller cell cannot. The expansion of the unstable regions in Figs. 7(a)–7(d) proves the importance of the active alignment to this self-organized system.

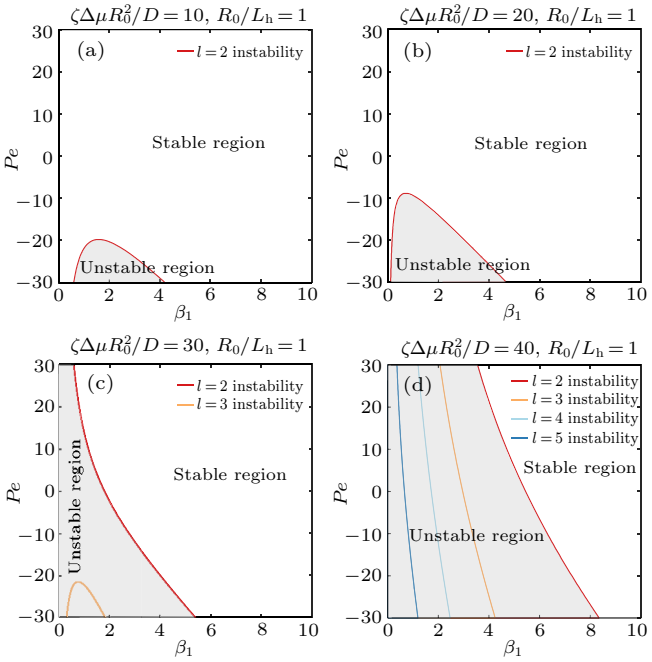


Fig. 6. The Pe–β_1 mode stability diagram.

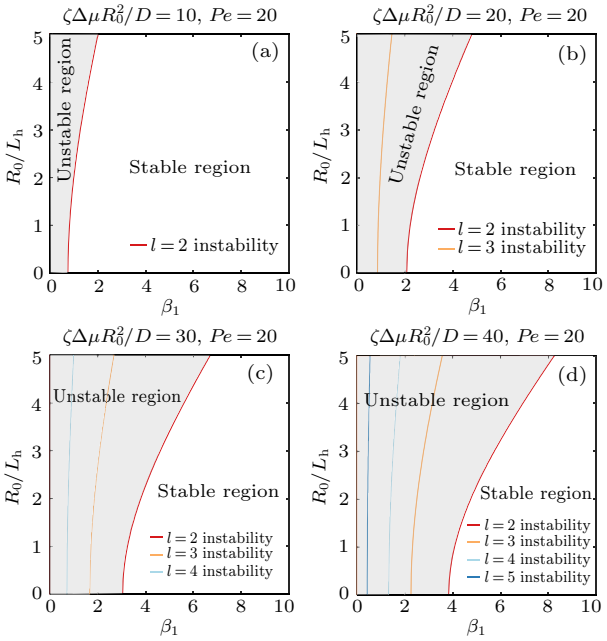


Fig. 7. The R_0/L_h–β_1 mode stability diagram.

5. Discussion

5.1. Strong contractility inhibits alignment of actin filaments

We have shown that strong contractility suppresses the $l = 2$ instability. This can be understood by analyzing the linearized nematic dynamics for the $l = 2$ mode:

$$\frac{\mathrm{d}\delta Q_{\mathrm{a}}^{(2)}}{\mathrm{d}t} = \frac{-2\beta_1\left(6\kappa + R_0^2\sigma\right)}{R_0^5\Gamma + 4R_0^3\eta_{\mathrm{s}}}\delta R^{(2)} + C\delta Q_{\mathrm{a}}^{(2)}, \quad (61)$$

$$\frac{\mathrm{d}\delta Q_{\mathrm{b}}^{(2)}}{\mathrm{d}t} = C\delta Q_{\mathrm{b}}^{(2)}, \quad (62)$$

where the constant C is given by

$$C = -\frac{K\left(4Ln^2 + A_1R_0^2\right)\left(R_0^2\Gamma + 4\eta_s + 2\beta_2\beta_1^2\right)}{R_0^2\beta_2\left(R_0^2\Gamma + 4\eta_s\right)} - \frac{2\beta_1\xi\Delta\mu f(\rho_0)}{R_0^2\Gamma + 4\eta_s} + \zeta\Delta\mu f(\rho_0). \tag{63}$$

From Eqs. (61) and (62), it follows that the excitation of $\delta Q_a^{(2)}$ and $\delta Q_b^{(2)}$ requires C to be positive. However, the second term in Eq. (63) indicates that contractile stress (i.e., $\xi > 0$) drives C toward negative values, thus suppressing the growth of nematic order. Active stress, given by $\xi\Delta\mu f(\rho)\boldsymbol{Q}$, depends both on $\xi\Delta\mu$ and the nematic tensor $\boldsymbol{Q}$. If an increase in $\xi\Delta\mu$ significantly reduces $\boldsymbol{Q}$, the active stress ultimately decreases as the nematic order $\boldsymbol{Q}$ approaches zero. Equation (63) also suggests that extensile stress ($Pe < 0$) increases C, promoting the growth of the nematic order $\delta Q_b^{(2)}$. This, in turn, gives rise to the chiral flow patterns, manifested by the growth of $\delta v_\phi^{(2)}$ in Fig. 4(b). To see the connection between the off-diagonal element of the nematic tensor $\delta Q_b^{(2)}$ and the chiral flow $\delta v_\phi^{(2)}$, we show the expression for the coefficient $\delta v_\phi^{(2)}$ associated with the chiral flow pattern $\boldsymbol{\Phi}_{20}$, which is derived from the force balance equation (32) in the tangential direction,

$$\delta v_\phi^{(2)} = \frac{-2R_0}{R_0^2\Gamma + 4\eta_s + 2\beta_2\beta_1^2}\left(\xi\Delta\mu f(\rho_0)\delta Q_b^{(2)} + \beta_1\beta_2\zeta\Delta\mu f(\rho_0)\delta Q_b^{(2)} - \beta_1\beta_2\frac{\mathrm{d}\delta Q_b^{(2)}}{\mathrm{d}t}\right). \tag{64}$$

Equation (64) clearly shows that the chiral flow $\delta v_\phi^{(2)}$ is motivated by $\delta Q_b^{(2)}$.

5.2. Anisotropic active stress alone cannot reproduce all the phenomenon observed in cell division

In this work, we consider only anisotropic active stress, given by

$$\boldsymbol{T}^a = \xi\Delta\mu f(\rho)\boldsymbol{Q}, \tag{65}$$

which is commonly adopted in studies on active nematic matter in flat space. Since $\boldsymbol{Q}$ is a traceless tensor, the stress components in the meridional and azimuthal directions have opposite signs,

$$(T^a)_u^u = -(T^a)_\phi^\phi. \tag{66}$$

This implies that if motors generate contractile stress in the azimuthal direction, they simultaneously induce extensile stress in the meridional direction and vice versa. Consequently, in our model, the nematic active stress alone struggles to drive meridional flows from the poles to the equator. When the cell is compressed at the equator due to contractile stress in the azimuthal direction, that is, $(T^a)_\phi^\phi > 0$, the resulting extensile stress in the meridional direction, $(T^a)_u^u < 0$, tends to push the flow away from the equator rather than towards it. This behavior is reminiscent of the flow patterns observed near pushers (extensile) and pullers (contractile) in active nematics (see Ref. [6]).

Furthermore, the divergence of the anisotropic active stress, $\mathrm{div}\,(\boldsymbol{T}^a)$, which appears in the force balance equations, consists of a tangential component

$$\boldsymbol{f}^t = \left[\xi\Delta\mu f(\rho)(\nabla_k Q_i^k) + \xi\Delta\mu\frac{\partial f(\rho)}{\partial s^k}Q_i^k\right]\boldsymbol{g}^i, \tag{67}$$

and a normal component

$$\boldsymbol{f}^n = -\xi\Delta\mu f(\rho)Q^{kl}C_{kl}\boldsymbol{n}. \tag{68}$$

In the axisymmetric case, the term $Q^{kl}C_{kl}$ is given by

$$Q^{kl}C_{kl} = Q_u^u\left(\frac{\psi'}{h} - \frac{\sin\psi}{r}\right), \tag{69}$$

which is proportional to the difference between the two principal curvatures. For a constricted sphere at the equator, the curvature term ψ'/h decreases, while $\sin\psi/r$ increases. As a result, we obtain

$$\left(\frac{\psi'}{h} - \frac{\sin\psi}{r}\right) < 0. \tag{70}$$

Consequently, if the active stress is contractile ($\xi > 0$), the normal component of the force, $\boldsymbol{f}^n$, points inward only if the filaments are aligned in the azimuthal direction, i.e., $Q_u^u < 0$.

Incorporating isotropic active stress into the model could resolve the problem of inconsistent flow directions. Since the isotropic active stress, $\boldsymbol{T}^{iso} = \xi^{iso}\Delta\mu f(\rho)\boldsymbol{G}$, is a symmetric tensor that satisfies

$$(T^{iso})_u^u = (T^{iso})_\phi^\phi, \tag{71}$$

allowing it to generate either contractile or extensile stress in both the meridional and azimuthal directions. Consequently, furrow constriction at the equator due to positive $(T^{iso})_\phi^\phi$ and flows from the poles toward the equator due to positive $(T^{iso})_u^u$ can occur simultaneously. However, isotropic active stress tends to trigger polarized instability ($l = 1$) with increasing ξ^{iso} before nematic instability ($l = 2$).[61] Consequently, the contractile ring tends to slide from the equator to the poles while constricting.[65]

The divergence of the isotropic active stress, $\mathrm{div}\,(\boldsymbol{T}^{iso})$, consists of a tangential component

$$(\boldsymbol{f}^{iso})^t = \xi^{iso}\Delta\mu\frac{\partial f(\rho)}{\partial s^k}g^{kj}\boldsymbol{g}_j, \tag{72}$$

and a normal component

$$(\boldsymbol{f}^{iso})^n = -\xi^{iso}\Delta\mu f(\rho)C_k^k\boldsymbol{n}. \tag{73}$$

If the active stress is contractile ($\xi^{iso} > 0$), the normal force points inward only if the mean curvature, C_k^k (the sum of the two principal curvatures), remains positive.

5.3. Biological implications

When examining how the stability of the system depends on the model parameters, we have identified the ratio R_0/L_h as a crucial dimensionless parameter. Our analysis reveals that as the cell size continuously decreases, the system transitions from an unstable state to a stable state, suggesting a loss of division capability. This finding is consistent with biological observations in *C. elegans* embryogenesis, where, after several rounds of cell division, the daughter cells gradually lose their ability to divide.[83,84] Our results provide a potential mechanistic explanation for this phenomenon, suggesting that the interplay between cell size and stability may play a fundamental role in the regulation of the cessation of cell division during development.

We emphasize that incorporating the nematic tensor into our model introduces several new parameters, including the elastic constants in the Landau–de Gennes energy (K, A_1, A_2 and L_n), as well as the flow-alignment coupling constant (β_1) and the active alignment strength (ζ). These phenomenological parameters are challenging to measure experimentally, which limits the quantitative predictive capacity of our results. In particular, for simplicity, we set all length scales, including L_H, L_K, and L_n, equal to the cell size R_0. However, the qualitative behavior of our key conclusions, such as the crucial role of active alignment in cell division, remains robust, as demonstrated by the analytical results of the linear stability analysis.

6. Conclusions

In this paper, we apply a hydrodynamic model of active surfaces to describe the surface deformation and cortical flows induced by molecular motors during cell division. The model can be applied to the cell cortex to investigate the emergence of two phenomena during cell division: the contractile ring and chiral flow. By solving the linearized dynamic equations, we show the time evolution of the perturbations of different modes. The $l=2$ instability is associated with the emergence of two phenomena during cell division: the contraction of the equator and chiral flows. We demonstrate that the active alignment is vital to the motivation of $l=2$ instabilities. With sufficiently strong active alignment, actin filaments are aligned azimuthally and the sphere tends to contract at its equator. Furthermore, we find that a strong contractile stress inhibits cell division by suppressing the nematic order and a strong extensile stress promotes the emergence of chiral flows with counter-rotating azimuthal flows in the two hemispheres. Our results provide a mechanistic explanation for the key phenomena observed during cell division, offering new insights into the role of active stress and filament alignment in cortical dynamics.

Appendix A: Scalar/vector/tensor spherical harmonics

We express the perturbation as a linear combination of spherical harmonic functions of different types. For the scalar field ρ, we expand it using the scalar spherical harmonic Y_{l0}, defined as

$$Y_{l0}=\sqrt{\frac{2l+1}{4\pi}}P_l(\cos\theta), \tag{A1}$$

where $P_l(x)$ denotes the Legendre polynomial.

For the vector field $\boldsymbol{v}$, we expand it using the vector spherical harmonic functions $\boldsymbol{\Psi}_{l0}=\Psi_i^{(l0)}\boldsymbol{g}^i$ and $\boldsymbol{\Phi}_{l0}=\Phi_i^{(l0)}\boldsymbol{g}^i$, with components given by

$$\Psi_i^{(l0)}=R_0\partial_i Y_{l0}, \tag{A2}$$

$$\Phi_i^{(l0)}=\epsilon^j{}_i\partial_j Y_{l0}. \tag{A3}$$

Here, $\boldsymbol{\Psi}_{l0}$ lies in the meridional direction and is curl-free, while $\boldsymbol{\Phi}_{l0}$ lies in the azimuthal direction and is divergence-free. In particular, the divergence-free vector field $\boldsymbol{\Phi}_{20}$ represents a chiral flow characterized by counter-rotating directions in the two hemispheres.

For the nematic tensor field $\boldsymbol{Q}$, we expand it using the tensor spherical harmonic functions $\bar{\boldsymbol{\Psi}}_{l0}=\Psi_{ij}^{(l0)}\boldsymbol{g}^i\otimes\boldsymbol{g}^j$ and $\bar{\boldsymbol{\Phi}}_{l0}=\Phi_{ij}^{(l0)}\boldsymbol{g}^i\otimes\boldsymbol{g}^j$, with components

$$\Psi_{ij}^{(l0)}=R_0\nabla_i\Psi_j^{(l0)}+\frac{1}{2}l(l+1)Y_{l0}g_{ij}, \tag{A4}$$

$$\Phi_{ij}^{(l0)}=\frac{1}{2}\left(\nabla_i\Phi_j^{(l0)}+\nabla_j\Phi_i^{(l0)}\right). \tag{A5}$$

There are four linearly independent tensor spherical harmonic functions; however, we select only two that satisfy the traceless and symmetric conditions required for the $\boldsymbol{Q}$ tensor. The tensor $\bar{\boldsymbol{\Psi}}_{l0}$ represents alignments either in the meridional or azimuthal direction, while $\bar{\boldsymbol{\Phi}}_{l0}$ describes a chiral alignment with projections in both meridional and azimuthal directions.

Acknowledgements

We acknowledge financial support from the National Natural Science Foundation of China (Grant No. 12474199) and the Fundamental Research Funds for Central Universities of China (Grant No. 20720240144), and 111 Project (B16029).

References

[1] Bechinger C, Di Leonardo R, Loewen H, Reichhardt C, Volpe G and Volpe G 2016 *Rev. Mod. Phys.* **88** 45006
[2] Agudo-Canalejo J and Nasouri B 2020 *Chin. Phys. B* **29** 064704
[3] Toner J and Tu Y 1998 *Phys. Rev. E* **58** 4828
[4] Mahault B, Ginelli F and Chate H 2019 *Phys. Rev. Lett.* **123** 218001
[5] Lauga E and Powers T R 2009 *Reports on Progress in Physics* **72** 096601
[6] Doostmohammadi A, Ignes-Mullol J, Yeomans J M and Sagues F 2018 *Nat. Commun.* **9** 3246
[7] Zhou Y, Li Y and Marchesoni F 2023 *Chin. Phys. Lett.* **40** 100505

[8] Saw T B, Doostmohammadi A, Nier V, Kocgozlu L, Thampi S, Toyama Y, Marcq P, Lim C T, Yeomans J M and Ladoux B 2017 *Nature* **544** 212
[9] Doostmohammadi A and Ladoux B 2022 *Trends in Cell Biology* **32** 140
[10] Wu H, de Leon M A P and Othmer H G 2018 *Journal of Mathematical Biology* **77** 595
[11] Juelicher F, Grill S W and Salbreux G 2018 *Reports on Progress in Physics* **81** 076601
[12] Salbreux G, Juelicher F, Prost J and Callan-Jones A 2022 *Phys. Rev. Research* **4** 033158
[13] Salbreux G and Juelicher F 2017 *Phys. Rev. E* **96** 032404
[14] Li M, Xing X, Yuan J and Zeng Z 2024 *Heliyon* **10** e29923
[15] Levayer R and Lecuit T 2012 *Trends in Cell Biology* **22** 61
[16] Brunet T 2023 *Current Biology* **33** R966
[17] Deserno M 2015 *Chemistry and Physics of Lipids* **185** 11
[18] Sheng J, Wang K Y, Ma B B, Zhu T and Jiang Z Y 2018 *Acta Phys. Sin.* **67** 158701 (in Chinese)
[19] Liao Y H, Zhu H C, Tang Z M and Huang K M 2015 *Chin. Phys. B* **24** 100204
[20] Zhong-can O Y and Helfrich W 1989 *Phys. Rev. A* **39** 5280
[21] Clark A, Dierkes K and Paluch E 2013 *Biophysical Journal* **105** 570
[22] Prost J, Juelicher F and Joanny J F 2015 *European Journal of Cell Biology* **11** 111
[23] Chugh P, Clark A G, Smith M B, Cassani D A D, Dierkes K, Ragab A, Roux P P, Charras G, Salbreux G and Paluch E K 2017 *Nature Cell Biology* **19** 689
[24] Fink A, Fazliev S, Abele T, Spatz J P, Goepfrich K and Cavalcanti-Adam E A 2024 *European Journal of Cell Biology* **103** 151428
[25] Werner M E, Ray D D, Breen C, Staddon M F, Jug F, Banerjee S and Maddox A S 2024 *Current Biology* **34** 3201
[26] Song W, He Q, Cui Y, Möhwald H, Diez S and Li J 2009 *Biochemical and Biophysical Research Communications* **379** 175
[27] Feierbach B and Chang F 2001 *Current Opinion in Microbiology* **4** 713
[28] Laporte D, Zhao R and Wu J Q 2010 *Seminars in Cell and Developmental Biology* **21** 892
[29] Stachowiak M, Laplante C, Chin H, Guirao B, Karatekin E, Pollard T and O'Shaughnessy B 2014 *Developmental Cell* **29** 547
[30] Pandya P, Orgaz J L and Sanz-Moreno V 2017 *Current Opinion in Cell Biology* **48** 87
[31] Laplante C, Berro J, Karatekin E, Hernandez-Leyva A, Lee R and Pollard T 2015 *Current Biology* **25** 1955
[32] Baldauf L, van Buren L, Fanalista F and Koenderink G H 2022 *ACS Synthetic Biology* **11** 3120
[33] Kondo T, Itakura S, Hamao K and Hosoya H 2012 *Experimental Cell Research* **318** 915
[34] Taneja N, Bersi M R, Baillargeon S M, Fenix A M, Cooper J A, Ohi R, Gama V, Merryman W D and Burnette D T 2020 *Cell Reports* **31** 107477
[35] Sun L, Guan R, Lee I J, Liu Y, Chen M, Wang J, Wu J Q and Chen Z 2015 *Developmental Cell* **33** 413
[36] Willet A H, McDonald N A and Gould K L 2015 *Current Opinion in Microbiology* **28** 46
[37] Hall A R, Choi Y K, Im W and Vavylonis D 2024 *Structure* **32** 242
[38] Di Cio S, Iskratsch T, Connelly J T and Gautrot J E 2020 *Biomaterials* **232** 119683
[39] Martín-García R, Arribas V, Coll P M, Pinar M, Viana R A, Rincón S A, Correa-Bordes J, Ribas J C and Pérez P 2018 *Cell Reports* **25** 772
[40] Somers W and Saint R 2003 *Developmental Cell* **4** 29
[41] Aspenstrom P 2008 *International Review of Cell and Molecular Biology* **272** 1
[42] Bashirzadeh Y, Moghimianavval H and Liu A P 2022 *iScience* **25** 104236
[43] Bathe M and Chang F 2010 *Trends in Microbiology* **18** 38
[44] Lebedev M, Chan F Y, Lochner A, Bellessem J, Osório D S, Rackles E, Mikeladze-Dvali T, Carvalho A X and Zanin E 2023 *Cell Reports* **42** 113076
[45] Cortes D B, Maddox P S, Nédéléç F J and Maddox A S 2023 *Biophysical Journal* **122** 3611
[46] Carim S C and Hickson G R 2023 *iScience* **26** 106903
[47] Ennomani H, Letort G, Guérin C, Martiel J L, Cao W, Nédélec F, De La Cruz E, Théry M and Blanchoin L 2016 *Current Biology* **26** 616
[48] Wu S K, Budnar S, Yap A S and Gomez G A 2014 *European Journal of Cell Biology* **93** 396
[49] Martin A C 2010 *Developmental Biology* **341** 114
[50] Arasada R and Pollard T 2014 *Cell Reports* **8** 1533
[51] Arbizzani F, Mavrakis M, Hoya M, Ribas J C, Brasselet S, Paoletti A and Rincon S A 2022 *Cell Reports* **39** 110722
[52] Founounou N, Loyer N and Le Borgne R 2013 *Developmental Cell* **24** 242
[53] Rizvi M S and Das S L 2012 *Journal of Theoretical Biology* **315** 139
[54] Carlton J G and Baum B 2023 *Current Opinion in Cell Biology* **85** 102274
[55] Sugioka K 2022 *Seminars in Cell and Developmental Biology* **127** 100
[56] Middelkoop T C, Garcia-Baucells J, Quintero-Cadena P, Pimpale L G, Yazdi S, Sternberg P W, Gross P and Grill S W 2021 *Proc. Natl. Acad. Sci. USA* **118** e2021814118
[57] de Kinkelder E M, Fischer-Friedrich E and Aland S 2023 *New J. Phys.* **25** 053034
[58] Salbreux G, Prost J and Joanny J F 2009 *Phys. Rev. Lett.* **103** 058102
[59] Bell S, Lin S Z, Rupprecht J F and Prost J 2022 *Phys. Rev. Lett.* **129** 118001
[60] Khoromskaia D, Salbreux G and Kozlov M M 2023 *eLife* **12** e75878
[61] Mietke A, Juelicher F and Sbalzarini I F 2019 *Proc. Natl. Acad. Sci. USA* **116** 29
[62] Mietke A, Jemseena V, Kumar K V, Sbalzarini I F and Juelicher F 2019 *Phys. Rev. Lett.* **123** 188101
[63] Mayer M, Depken M, Bois J S, Juelicher F and Grill S W 2010 *Nature* **467** 617
[64] Torres-Sánchez A, Millán D and Arroyo M 2019 *Journal of Fluid Mechanics* **872** 218
[65] Gao D, Sun H, Ma R and Mietke A 2025 *Preprint* arXiv: 2501.17849
[66] Onsager L 1949 *Annals of the New York Academy of Sciences* **51** 627
[67] Pathria R and Beale P D 2011 15-fluctuations and nonequilibrium statistical mechanics *Statistical Mechanics (Third Edition)* (Boston: Academic Press) pp. 583–635
[68] Bement W M 2002 *Current Biology* **12** R12
[69] Backouche F, Haviv L, Groswasser D and Bernheim-Groswasser A 2006 *Physical Biology* **3** 264
[70] Schuppler M, Keber F C, Kroger M and Bausch A R 2016 *Nat. Commun.* **7** 13120
[71] Dean S O, Rogers S L, Stuurman N, Vale R D and Spudich J A 2005 *Proc. Natl. Acad. Sci. USA* **102** 13473
[72] Kreyszig E 1991 *Differential Geometry* (New York: Dover)
[73] Yang P and Tu Z C 2016 *Acta Phys. Sin.* **65** 188701 (in Chinese)
[74] Liang Y F and Zhang S G 2017 *Acta Phys. Sin.* **66** 158701 (in Chinese)
[75] Ji D D and Zhang S G 2018 *Acta Phys. Sin.* **67** 188701 (in Chinese)
[76] Zhang P W and Shi A C 2015 *Chin. Phys. B* **24** 128707
[77] Wei T, Zhang L and Zhang Y 2020 *Chin. Phys. B* **29** 048702
[78] Liang Y R and Liang Q 2019 *Acta Phys. Sin.* **68** 028701 (in Chinese)
[79] Li S L and Zhang S G 2010 *Acta Phys. Sin.* **59** 5202 (in Chinese)
[80] Zhang Y H, McDargh Z and Tu Z C 2018 *Chin. Phys. B* **27** 038704
[81] Gennes P G D and Prost J 1993 *The Physics of Liquid Crystals* (Oxford University Press)
[82] Sedzinski J, Biro M, Oswald A, Tinevez J Y, Salbreux G and Paluch E 2011 *Nature* **476** 462
[83] Sulston J and Horvitz H 1977 *Developmental Biology* **56** 110
[84] Sulston J, Schierenberg E, White J and Thomson J 1983 *Developmental Biology* **100** 64